Central Lancashire Online Knowledge (CLoK)

Title	Computational Fluid Dynamic Studies of Vortex Amplifier Design for the Nuclear Industry—II. Transient Conditions
Type	Article
URL	https://clok.uclan.ac.uk/7421/
DOI	https://doi.org/10.1115/1.4005950
Date	2012
Citation	Francis, Jonathan, Birch, Martin John and Parker, D. (2012) Computational Fluid Dynamic Studies of Vortex Amplifier Design for the Nuclear Industry—II. Transient Conditions. Journal of Fluids Engineering, 134 (2). 021103. ISSN 00982202
Creators	Francis, Jonathan, Birch, Martin John and Parker, D.

Computational Fluid Dynamic Studies of Vortex Amplifier Design for the Nuclear Industry—II. Transient Conditions

J. Francis
e-mail: jfrancis1@uclan.ac.uk

M. J. Birch
e-mail: mjbirch@uclan.ac.uk

John Tyndall Institute for Nuclear Research,
UCLan | Nuclear,
School of Computing, Engineering and Physical
Sciences,
University of Central Lancashire,
Preston PR1 2HE, UK

D. Parker
John Tyndall Institute for Nuclear Research,
UCLan | Nuclear,
School of Computing, Engineering and Physical
Sciences,
University of Central Lancashire,
Preston, UK;
Telereal Trillium,
140 London Wall,
London EC2Y 5DN, UK
e-mail: darren.parker@telerealtrillium.com

In this paper computational fluid dynamics (CFD) techniques have been used to investigate the effect of changes to the geometry of a vortex amplifier (VXA) in the context of glovebox operations in the nuclear industry. These investigations were required because of anomalous behavior identified when, for operational reasons, a long-established VXA design was reduced in scale. The study simulates the transient aspects of two effects: back-flow into the glovebox through the VXA supply ports, and the precessing vortex core in the amplifier outlet. A temporal convergence error study indicates that there is little to be gained from reducing the time step duration below 0.1 ms. Based upon this criterion, the results of the simulation show that the percentage imbalance in the domain was well below the required figure of 1%, and imbalances for momentum in all three axes were all below measurable values. Furthermore, there was no conclusive evidence of periodicity in the flow perturbations at the glovebox boundary, although good evidence of periodicity in the device itself and in the outlet pipe was seen. Under all conditions the modified geometry performed better than the control geometry with regard to aggregate reversed supply flow. The control geometry exhibited aggregate nonaxisymmetric supply port back-flow for almost all of the simulated period, unlike the alternative geometry for which the flow through the supply ports was positive, although still nonaxisymmetric, for most of the period. The simulations show how transient flow structures in the supply ports can cause flow to be reversed in individual ports, whereas aggregate flow through the device remains positive. Similar to the supply ports, flow through the outlet of the VXA under high swirl conditions is also nonaxisymmetric. A time-dependent reverse flow region was observed in both the outlet and the diffuser. It is possible that small vortices in the outlet, coupled with the larger vortex in the chamber, are responsible for the oscillations, which cause the shift in the axis of the precessing vortex core (and ultimately in the variations of mass flow in the individual supply ports). Field trials show that the modified geometry reduces the back-flow of oxygen into the glovebox by as much as 78%. At purge rates of 0.65 m^3/h the modified geometry was found to be less effective, the rate of leakage from the VXA increasing by 16–20%. Despite this reduced performance, leakage from the modified geometry was still 63% less than the control geometry. [DOI: 10.1115/1.4005950]

1 Introduction

The United Kingdom Atomic Energy Authority was one of the first U.K. organizations to recognize the potential of power fluidics in process control. Power fluidics is the name given to the control of liquids or gases without the use of moving parts. One application, which clearly demonstrates the benefit of power fluidics over conventional electropneumatic systems, was the use of vortex amplifiers (VXAs) in the pressure control and protection of gloveboxes. The nuclear industry uses gloveboxes as a means of allowing personnel to undertake potentially hazardous operations, simultaneously ensuring that no contact is made with the material being handled. Under normal operating conditions subatmospheric pressures of 250–500 Pa are maintained within the glovebox. With the exception of overall scale changes and external modifications to exit port arrangements, the internal design of

VXAs used at the Sellafield site has hardly changed for more than two decades.

The most recent type of VXA used at Sellafield is a geometrically reduced version of earlier units. This *mini-VXA* is approximately half the size of its predecessor, the reduction having been made because of ergonomic restrictions in the process plant installations. The Eulerian similitude of the VXA [1] meant that simple square law calculations could be used to scale the new units. Unlike some of their predecessors, the mini-VXAs are mounted directly onto the glovebox with the supply ports open to the glovebox environment. An inert gas purge is used to reduce the risk of fire and to control moisture levels within the glovebox. Oxygen levels within the glovebox are maintained at no more than 9% by volume, although the exact specification depends upon various factors and can sometimes be lower to minimize moisture levels. Inert gas purging rates are set to maintain this level under normal operating conditions (but, significantly, not under emergency breach conditions). Once removed from the glovebox via the VXA, the gas cannot be recirculated and is carried away by the main extract system before being filtered and then discharged to

atmosphere. The principle of operation of the VXA is explained in the accompanying paper [2], hereafter referred to as "Paper1."

Despite a lengthy design, installation, and commissioning process, performance of the scaled mini-VXA units has been disappointing. Standard supply flow rates of inert gases have had to be increased to maintain the 9% oxygen limit. Investigations by Zhang [3] have confirmed the high oxygen levels in the glovebox and have identified the possibility that the increase of oxygen is caused by the back-flow of incoming air from the VXA control ports through the supply ports into the inerted glovebox.

The primary purpose of this research was to apply flow visualization and CFD techniques to elucidate and understand the complex three-dimensional flows that influence the performance of the mini-VXA (subsequently, "the VXA"). In doing so, the ultimate objective was to develop a prototype VXA unit capable of reducing air leakage back into the glovebox without the use of an additional structure such as a cowl or distancing chamber, and hence to reduce the cost of keeping a glovebox inerted. Following a study of steady-state flows in various candidate geometries (see Paper1 [2]) a prototype geometry was established that, when physically tested on site, reduced inert gas usage to 25% of the scaled mini-VXA units [4].

The Baseline (BSL) turbulence model was used in the steady-state investigations of Paper1 [2] and the resulting flow structure and convergence appeared to capture evidence of the known precessing vortex core, along with nonaxisymmetric boundary flows in the chamber and exit port. That result implied that the flow structures in the four inlet ports were not identical, but affected by the vortex. The primary aim of this second paper is to confirm that in transient solutions there is evidence of periodic changes in flow structure within the inlet ports that are of significant magnitude to affect local oxygen content at the four entrances to the VXA, and which can be associated with the precession of the vortex core in the exit port. A second aim is to further investigate the ability of the BSL turbulence model in producing near-wall flow structures in the narrow inlet ports and vortex chamber, without excessive free stream effects.

Numerous computational fluid dynamic (CFD) studies of vortex flows in burners and centrifugal separators have been carried out, with considerable success [5–7]. By comparison little has been published on the simulation of flows through VXAs, some notable exceptions being Refs. [8–10]. To facilitate the objectives of this investigation, a series of experiments and simulations have been undertaken to understand better the physics of radial VXAs and their characteristic behavior. Physical experiments have been conducted for over 30 geometric variations; smoke visualization and air tests were used to investigate VXA operating characteristics

and complex time-dependent fluidic flow structures responsible for the back-diffusion of oxygen into the glovebox. A CFD modeling and simulation study was then carried out on a subset of these geometries with the aim of improving the design of the VXA. Specifically, the objectives of the simulation study were: (i) to simulate fluid flow within the VXA, capturing the specific flow phenomena that are known to exist within thin vortex chambers when operated under high swirl conditions; (ii) to reproduce the observed phenomena of air/oxygen back-flow through the VXA supply ports and recirculation of the vortex core in the exit port; and (iii) to assess the performance of the alternative supply port geometries with respect to their ability to reduce or prevent the back-flow phenomenon.

The results of smoke and air experiments, the modeling of the VXA geometry, the verification and validation of the computational mesh, and the results of the steady-state CFD simulations have been documented in Paper1 [2]. Although the results of these simulations successfully reproduced the required steady-state behavior in both the supply and outlet ports, temporal flow regimes within these regions were not resolved. Moreover, asymmetric results between the four supply ports and a helical flow structure in the outlet pipe hint at important transient phenomena. Transient CFD simulations were therefore used to elucidate further evidence of asymmetry and to qualitatively assess the probable cause. The purpose of these transient CFD simulations is to predict the complex flow structures within the VXA, that is, to model the state of the system under geometrical conditions for which the CFD model has not been experimentally validated. This paper reports on the transient behavior predicted in the inlet ports and summarizes the development of an alternative prototype.

2 Modeling the Mini-VXA

The VXA consists of a thin cylindrical chamber through which flow is introduced via four radial supply ports. The flow travels radially into the chamber before exiting perpendicular to the plane of the cylinder via a hole, the exit port, in the end plate. Modulation of the chamber vortex is achieved through four control ports fitted tangentially around the periphery of the chamber. A detailed description of the geometry is given in Paper1 [2].

In an attempt to prevent or forestall bifurcated back-flow passing along the supply port wall, a notched taper was added to the wall of each supply port (varying the width of each supply port, simultaneously keeping all other geometrical parameters fixed). Figure 1 shows a simplified planar view of the VXA arrangement and inserts; dimensions of all the geometries modeled are given in Table 1.
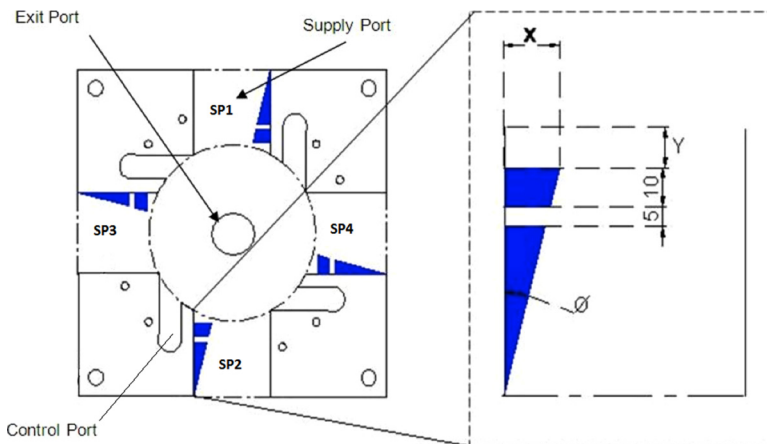
Fig. 1 Simple diagram of VXA geometry, showing the proposed modifications in blue (The ordering of supply ports SP1–4 around the chamber is shown in the left-hand panel.)

Table 1 Geometric parameters

Dimensions[a]				
A_e (mm^2)	A_c (mm^2)	r_0 (mm)	r_e (mm)	h (mm)
660.6	760	69.9	14.5	11.4

VXA geometrical variations[b]				
Geometry	A_s (mm^2)	X (mm)	Y (mm)	ϕ (deg)
7.0	2600	0	0	0.00
1.1	2400	5	0	4.25
1.4	2400	5	30	7.49
2.2	2200	10	10	10.68
2.3	2200	10	20	11.77
3.1	2000	15	0	12.44
3.2	2000	15	10	14.50
3.3	2000	15	20	17.35
3.4	2000	15	30	21.45

[a]A_e: area of exit port; A_c: area of control ports; r_0: vortex chamber radius; r_e: exit port radius; and h: height of vortex chamber.
[b]A_s: area of supply ports; see Fig. 1 for X, Y, and ϕ.

2.1 Temporal Convergence Error. A second-order backward Euler scheme was adopted for the transient study reported here and the simulation started from the steady-state results (see Paper1 [2]). Total simulation time was set at 5×10^{-3} s.

A temporal convergence error study was carried out for the selected geometries to establish the influence of the time-step duration on mass flow rates. Each geometry was tested using four time-step lengths of 5×10^{-5} s, 1×10^{-4} s, 2×10^{-4} s, and 5×10^{-4} s.

Results from the spatial validation (Paper1 [2]) were used to inform the choice of geometry for the temporal validation. The results of the previous spatial error study showed that steady-state results became independent of mesh resolution when the number of elements in the model approached 2×10^6. Computational meshes 7.0(b), 1.1(b), 1.4(b), 3.1(b), and 3.4(b) were used to assess the temporal discretization error. Table 2 lists the numbers of elements and nodes in the computational meshes for each geometry modeled.

An entrained flow setting with fully formed turbulence was used to describe the opening at the control and exit ports. The pressure differential between exit and supply port was held at 150 Pa. The control pressure was based on the point in the characteristic where the aggregate flow started to reverse. Entry to the inlet port from the glovebox is sharp-edged, but the inlet port enters the vortex chamber by means of two radiused walls and two continuous walls.

Figure 2 shows the results of the temporal error discretization study for the outlet port mass flow rate W_O; similar results were produced for the supply and control port values (not shown). The largest value of A_{rms}, that for W_C, was less than 1.2%; this value was based upon the difference between the largest and smallest time steps. Overall, the value of A_{rms} varied little over the range of time steps investigated, the largest variation being 0.16%. Results of the temporal error discretization study indicated that there was little to be gained from reducing the time-step duration

Table 2 VXA geometry computational mesh details

VA geometry	Number of elements	Number of nodes
7.0(b)	2,155,748	660,515
1.1(b)	2,142,522	573,428
1.4(b)	2,193,520	672,736
3.1(b)	2,106,747	563,881
3.4(b)	2,165,524	663,641
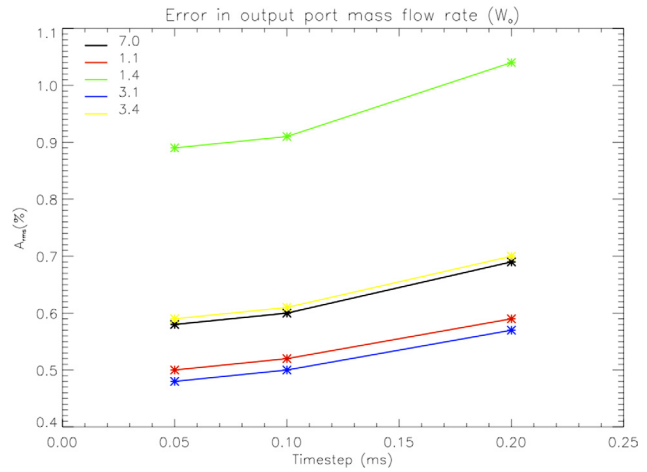
Fig. 2 Error in outlet port mass flow rate (W_o) for a given physical time step, for each geometry

below 0.1 ms. Results of the above investigations were used to inform subsequent simulations. The mesh length scales, residual convergence criteria and time-step durations were all based upon the verification and validation exercises in Paper1 [2].

2.2 Predictive Use. Following the study of temporal discretization error mentioned previously, during predictive simulation (i) the time step in each case was 1×10^{-4} s or less and (ii) the number of internal coefficient loops reached between 10 and 12 per time step. The time step was established using the ANSYS solver, based on a residual convergence criteria of 1×10^{-5}, with an imbalance of less than 1%. Care was taken to ensure that the time step chosen was not so small as to elucidate flow regimes and periodicity not relevant to the investigation. Previous researchers using flow visualization studies reported a precessing vortex with its frequency in the region of 50–60Hz (e.g., Ref. [11]). A physical time step of 1×10^{-4} s is adequate to capture 16–20 points in a cycle of that frequency, and is therefore considered sufficient to elucidate qualitative evidence of an association between supply port structure and a precessing vortex.

As in Paper1 [2], turbulence was simulated using the BSL Reynolds stress model, used in conjunction with a BSL omega equation, as described in Refs. [12,13]. This turbulence model is a combination of the standard k–ε model and the k–ω model of Refs. [14,15]. The standard k–ε model uses standard values for coefficients encountered in equations representing kinetic energy generation and dissipation, as developed from the classical work by Launder and Spalding [16]. It is known to give good approximation well away from physical boundaries and reasonable predictions of separated shear flows with square-edged geometries. However, it overpredicts turbulent energy in near-wall flows and fails to reproduce anisotropy of strain and Reynolds stresses in conditions of high swirl, such as one would expect to encounter in the curved geometry of the vortex amplifier chamber. In contrast, the k–ω model gives a good approximation close to physical boundaries, but is more sensitive to initial free stream boundary conditions.

The BSL Reynolds stress model used in the ANSYS CFX software (CFX) includes the best features of both the k–ε and k–ω models. It is a hybrid model, with blending functions controlling turbulent properties between the best domains of each. Selection of the "baseline" BSL model enables simulation of turbulent effects through the boundary layer, right down to the viscous sublayer and, in this case, right down through the wall elements of the narrow inlet port and swirl chamber. However, as one moves away from the wall with increasing y+ values affecting element size, blending functions allow reversion to the k–ε model. By the use of this model, the automatic wall treatment switches smoothly

Table 3 Transient simulation control port boundary conditions for the geometries to be tested

VXA geometry	P_c (Pa)
7.0	−373.0
2.2	−371.5
2.3	−372.0
3.2	−372.0
3.3	−372.5

from the use of turbulent wall functions to natural wall boundary conditions as the mesh is refined to sufficiently small values. By this means the intention was to capture anisotropic strain (or fluidic pressure effects).

The shear stress transport (SST) turbulence model is considered to be an improvement on BSL, where external curvature creates adverse pressure gradients, by placing limiting conditions on eddy viscosity predictions. However, it is not capable of capturing anisotropic turbulent stresses, so it was not utilized here. The BSL Reynolds stress model is not new but its use has been restricted until recently by the high computational power it requires (compared to SST). In the current application the ability to capture anisotropic effects was considered important in providing predictive results.

Boundary conditions for the models were specified using static and total pressures and using a nonslip condition at physical walls. The glovebox opening was set to a total pressure of −385 Pa, with flow normal to the boundary. Turbulence across the boundary was assumed to be low (~1% intensity, with a viscosity ratio equal to 1). The exit port outlet was given a static entrained pressure of −535.5 Pa. When specifying relative pressures at "openings" the CFX solver assumes that if fluid is pushed out of the domain across the boundary then the pressure specified is static. The entrained pressure option is recommended for situations where flow is drawn across a boundary, the flow direction being calculated from the direction of the velocity field. Fully developed turbulence conditions were assumed for the outlet, with the boundary condition set to "zero gradient." A static, entrained pressure condition of −376 Pa was fixed for the control port inlets.

3. Results of the Transient Simulation

In order to understand better the effects of the vortex core and control port streams on supply port temporal performance, several transient simulations were carried out, based upon the time step criteria verified in Sec. 2. The boundary conditions for the study were specified using a range of pressure readings in which the pressure differential between the supply and exit ports (P_{se}) was held constant at 150 Pa. The control port pressure (P_c) was based upon the point at which aggregate flow through the supply port geometries started to reverse. The control port pressures used for each of the geometries under test are given in Table 3.

Each transient simulation commenced from a steady-state solution. Relaxation of the convergence criteria was used as a means of reducing the computational time taken to simulate the developing flow through the VXA until the quasi-steady state was achieved.

Throughout the simulation the maximum residuals for momentum converged well before the target values were attained. However, the maximum mass residual usually required one additional internal coefficient loop before meeting the residual convergence criteria. Values for percentage imbalance in the domain were well below the target figure of 1%. Imbalances for momentum in all three axes were all below measurable values. The only recordable values were those for mass, the largest recorded imbalance being 0.0003%.

3.1 Global Flow Perturbations. Figures 3 and 4 show the quasi-steady time-dependent mass flow through the glovebox boundary. Figure 3 shows the mass flow rates at the control and outlet ports for geometries 7.0 (the control geometry) and 2.2 (the best performing alternative supply port geometry). Figure 4 shows the mass flow rate at the supply ports for these same geometries, based upon the flow across the glovebox boundary, not the aggregate flow at the VXA supply ports (on which the steady-state results were based in Paper1 [2]).

Figures 3 and 4 demonstrate that there is no persistent periodicity in the flow perturbations being generated at the domain boundaries. It is possible that a fundamental periodicity would eventually establish itself if the simulations were allowed to continue. Results from the steady-state simulations presented in Paper1 [2] indicate that the periodicity may begin as much as 0.5 s after the quasi-steady state has been reached. For a given geometry, operating under similar high swirl conditions, this estimate is based upon the duration of the automatic time step calculated by the solver for convergence to a steady-state solution. Due to computing constraints, further transient simulations over a longer period of time were beyond the scope of this study.

In Fig. 3 the values of W_o and W_c for geometry 7.0 appear to fall until the simulation time of 0.225 s is reached, whereas for
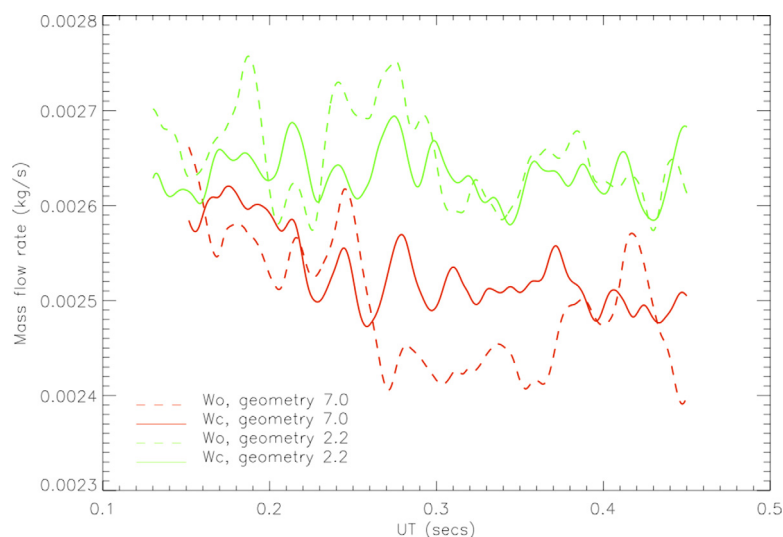
Fig. 3 Transient variation of control and output port mass flow rates for geometries 7.0 and 2.2
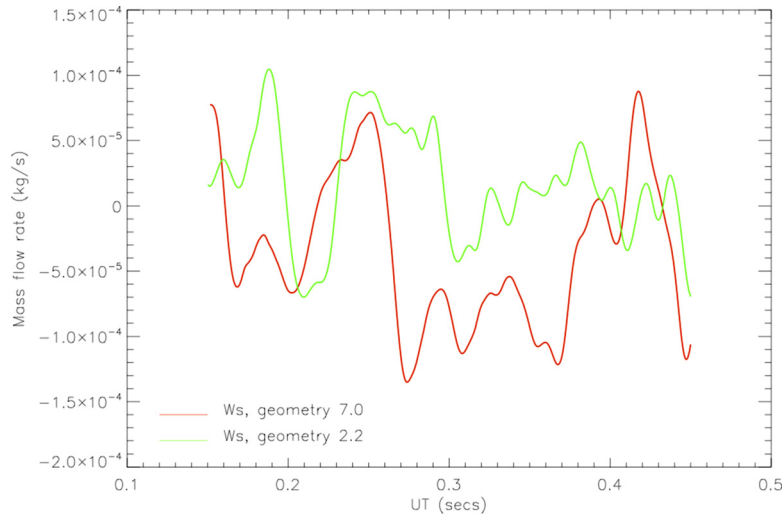
Fig. 4 Transient variation of supply port mass flow rate for geometries 7.0 and 2.2

geometry 2.2 these parameters remain quasi-stable. By this time it is possible that, unlike geometry 2.2, geometry 7.0 had yet to achieve a quasi-steady state. However, the overall perturbation in both control port and total flow is small compared to the quasi-steady magnitude previously achieved.

In Fig. 4, it is evident that, on average, the aggregate flow (W_s) across the glovebox boundary for geometry 7.0 is mainly reversed, whereas for geometry 2.2 reverse flow occurs far less frequently, and at a reduced magnitude (despite the increased pressures across the control ports of geometry 2.2). In fact, over the period of time shown in Fig. 4, the average value of W_s predicted at the glovebox boundary for geometry 7.0 was approximately half that calculated for the same pressures at the supply ports under steady-state conditions. That for geometry 2.2 is an approximate match for the equivalent steady-state results which, when coupled with the initial fall in flow rate for geometry 7.0 in Fig. 4, is attributed to the overall time of simulation, where to capture the full amplitude and frequency of any cyclic effect may require prolonged simulation times.
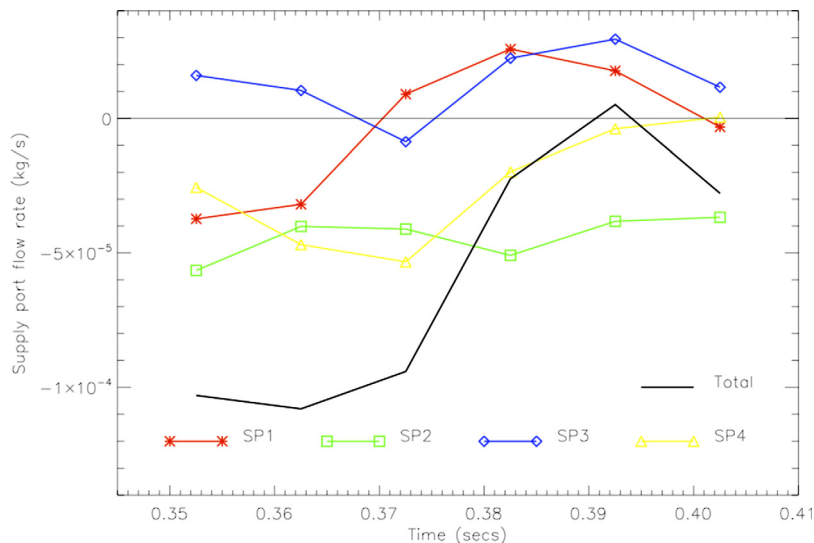
The average supply port mass flow rates for geometry 2.2 shown in Fig. 4 were better than those predicted by the steady-state simulations. Despite the variation in flow rates it is clear

that, even at elevated control port pressures, the alternative supply port geometry (2.2) performs better than the control geometry (7.0) with respect to reversed supply flow.

Although aggregate flow rates provide a reasonable indication of the performance of the VXA, they neither capture the asymmetric effects of simultaneous flow in and out of a single supply port, nor do they show the range of inflow and outflow rates possible across the four supply ports, neither spatially nor temporally.

3.2 Transient Supply Port Asymmetry. Although the flow across the glovebox boundary provides a good indication of aggregate supply port performance, it offers little information about the asymmetry of the device. Comparing the transient mass flow rate data for each supply port with (i) exit port contour plots, and (ii) supply port vector plots over the same period, provides greater insight into the effect that transient flow structures have on VXA performance.

Figures 5–9, which are based upon behavior in the midplane of the supply port ($z = -5$ mm), depict this asymmetric flow for geometries 7.0 and 2.2. Figures 5 and 7 show graphically how the mass flow rates vary for geometries 7.0 and 2.2 through each of the supply ports SP1 to SP4 over a brief period of time

Fig. 5 Transient supply port mass flow rate (W_s) through the supply ports for geometry 7.0 ($P_c = -373$ Pa: $z = -5$ mm)

Journal of Fluids Engineering
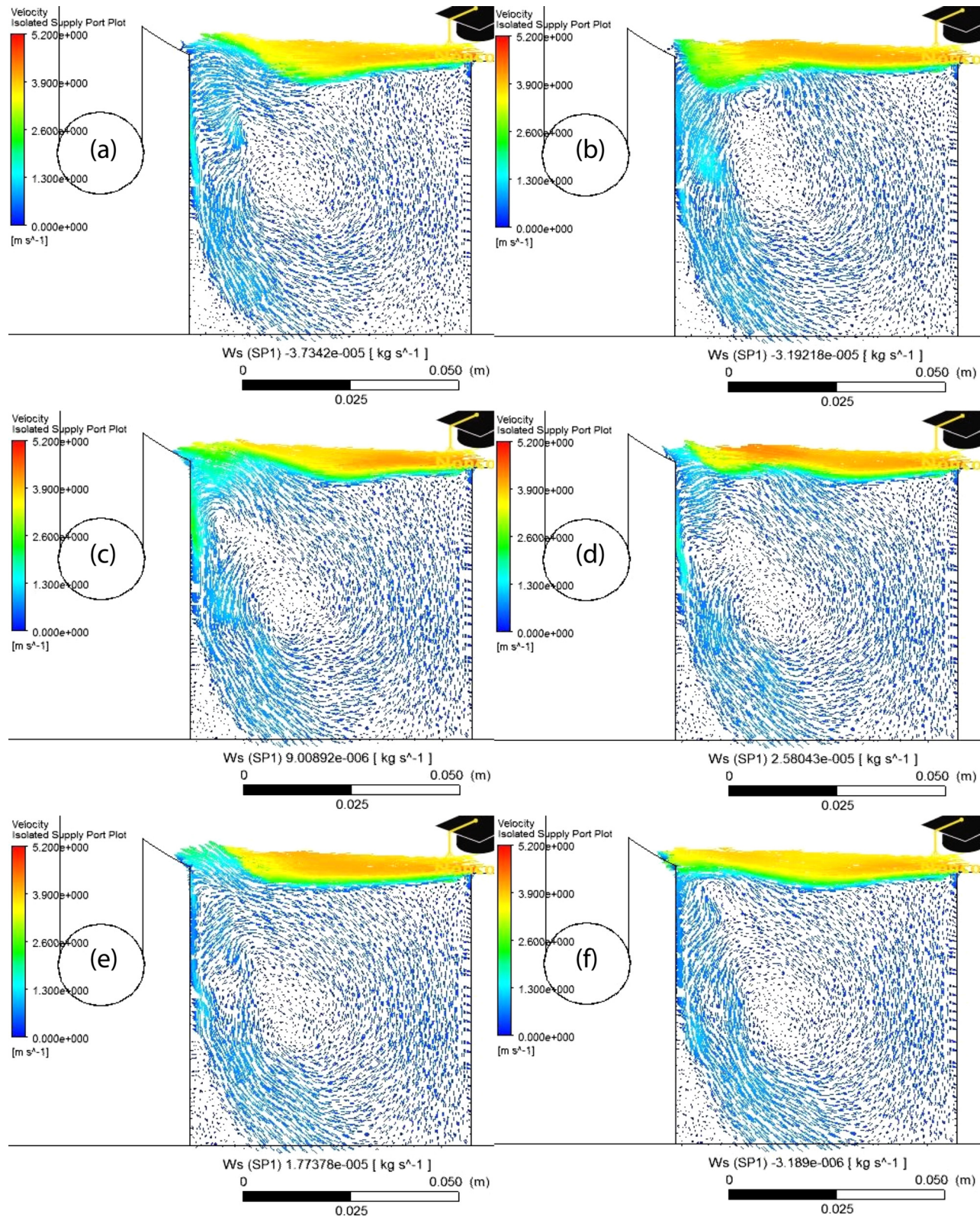
Fig. 6 Velocity vectors, geometry 7.0, SP1 ($P_c = -373$ Pa: $z = -5$ mm): (a) 0.352 s; (b) 0.362 s; (c) 0.372 s; (d) 0.382 s; (e) 0.392 s; (f) 0.402 s

($\sim$0.35–0.42 s). Some supply ports exhibit back-flow (negative W_s), whereas the aggregate flow through the VXA can still be positive. The transient vector plots of supply port SP1 depicted in Figs. 6 and 8 for geometries 7.0 and 2.2 were recorded every 100 time steps (the period over which each figure is plotted varies slightly because the solver was set to adaptive time stepping).

Figure 9 depicts a similar vector plot, that for supply port SP4 of geometry 2.2 under the same conditions. The actual mass flow rates are displayed at the bottom of each vector plot; the values relate to those in Figs. 5 and 7.

(Note: In Figs. 6, 8, and 9 back-flow into the glovebox is represented by "downward" vectors. Further, because of the orientation
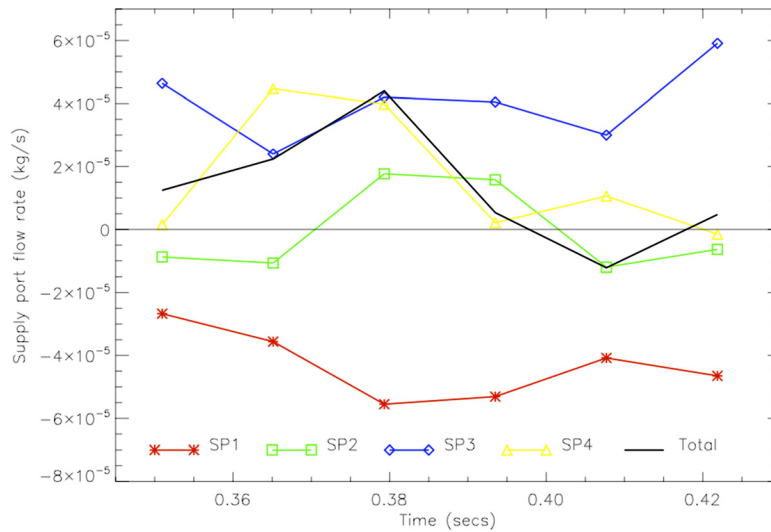
Fig. 7 Transient supply port mass flow rate (W_s) through the supply ports for geometry 2.2 ($P_c = -371.5$ Pa: z = −5 mm)

of supply port 4 with respect to the simulation axes (not shown), the sign of W_s in Fig. 9 is opposite to that plotted in Fig. 7, although, of course, the magnitude is unchanged.)

Careful study of the flow patterns in SP1–SP4 for geometry 7.0 (Figs. 5 and 6) show a peculiar situation. The apparently symmetric geometry produces asymmetric supply port flow structures. The total flow rate in all four supply ports shows evidence of being cyclic. However, though the flow in SP3 is almost entirely positive, that in SP2 & SP4 is entirely reversed, and in SP1 it changes from negative to positive. The overall pattern is one of a cyclic negative flow, but the four ports are behaving very differently. This imbalance in port flow rates and intimation of cyclic effect is considered to be evidence of a precessing vortex core and variable attachment position in the chamber and outlet pipe. However, it is important to note that the cyclic influence may simply be a periodic effect superimposed on an already asymmetric flow structure in the four supply ports generated through fluidic effects.

In Fig. 5 flow through SP1 varies from -3.73×10^{-5} kg/s to 2.58×10^{-5} kg/s (average $W_s = -3.32 \times 10^{-6}$ kg/s). The range of flow through SP1 is large, as is the range of the aggregate flow through the VXA, which varies from -1.08×10^{-4} kg/s to 5.13×10^{-6} kg/s (average $W_s = -5.85 \times 10^{-5}$ kg/s). For almost all of the period shown in Fig. 5 aggregate supply flow through the VXA is reversed, with only a very short period of positive flow at ∼0.392 s. Despite this, flow through SP1 is positive from 0.372 s to 0.402 s.

In Fig. 6, an area of recirculation with a reverse-flow component appears to have formed within SP1 at t = 0.362 s. The top of the recirculation is forced to the left of the supply port opening by the faster-moving control port fluid stream. This causes pressure at the top left of the supply port to increase. As the pressure builds, the control flow stream is pushed upward and away from the supply port wall, back toward the vortex chamber. Fluid from the supply port stream is then drawn in through the opening to reverse the aggregate direction of flow through the port. However, positive flow can be seen in the vector plots from 0.372 s to 0.392 s; eventually the increased supply flow through the gap leads to a reduction in static pressure at the top left corner of the control port, the reduced pressure once more allowing the control port stream to cut off supply flow and effectively reverse it.

The behavior of geometry 2.2 in Figs. 7–9, in which the velocity through SP1 varies between -5.55×10^{-5} kg/s and -2.67×10^{-5} kg/s (average $W_s = -4.3 \times 10^{-5}$ kg/s), differs markedly from that of geometry 7.0 in Figs. 5 and 6. The range of velocity through SP1 is less than that for geometry 7.0. The aggregate supply velocity varied from -2.43×10^{-5} kg/s to 4.41×10^{-5} kg/s (average $W_s = 1.37 \times 10^{-5}$ kg/s). For the majority of the period shown in Fig. 7 aggregate supply flow through the VXA and supply ports SP3 and SP4 is positive, the period of aggregate reverse flow being from about 0.40 s to 0.42 s. However, flow through SP1 is clearly reversed throughout this period. This result is unusual in that flow through SP3 remained positive over the whole period, whereas that through SP1 remained negative. Although it is not clear in the vector plots for SP1, the same area of recirculated flow was seen to develop in the top left corner of the supply port stream in supply ports SP2 and SP4. In both instances the area of recirculation was confined by the converging taper, increasing the pressure generated and forcing the control port fluid stream away from the supply port wall (Fig. 8).

Figure 9 shows a set of vector plots of SP4 for modified geometry 2.2 for the same period of time. At t = 0.351 s the area of recirculation is starting to form. As before, a negative value indicates back-flow into the VXA supply port (and ultimately into the glovebox), a positive value indicates out-flow. At 0.365 s the strength of the recirculation area has increased, allowing more fluid to pass into the device; the diversion of the fast control flow stream is clear at the top left of the plot. It is also interesting to note that the area of recirculation has extended horizontally from left to right across the top of the port. The same action can be seen in the plots at 0.379 s and 0.393 s; this is not dissimilar to the flow formations identified during the smoke tests in Paper1 [2].

As the area of recirculation extends across the supply port opening it appears to weaken and is eventually overcome by the control port flow stream; at 0.422 s the force of the control flow stream is such that it has expelled the area of recirculation from the corner formed by the taper. This effectively closes the supply port causing flow through the port to reverse. The cycle is then repeated as flow at the top of the port is entrained by the faster moving control port stream and forced into the corner, resulting in the formation of a high pressure recirculating region, which diverts the control port stream and allows positive flow through the supply port.

Similar areas of recirculation and back-flow were witnessed during physical investigations carried out by Chow [17] and Blanchard [18]. Chow carried out experimental investigations into VXA characteristics using water as a test medium; dye traces fed into the supply inlets of the VXA were used to delineate internal flow patterns. In describing the test procedure Chow explained how he used the reversed flow pattern in the supply manifold as a means of identifying when supply flow had been blocked. Blanchard also carried out visualization studies using small threads attached to pins inserted in the end wall of a previous VXA
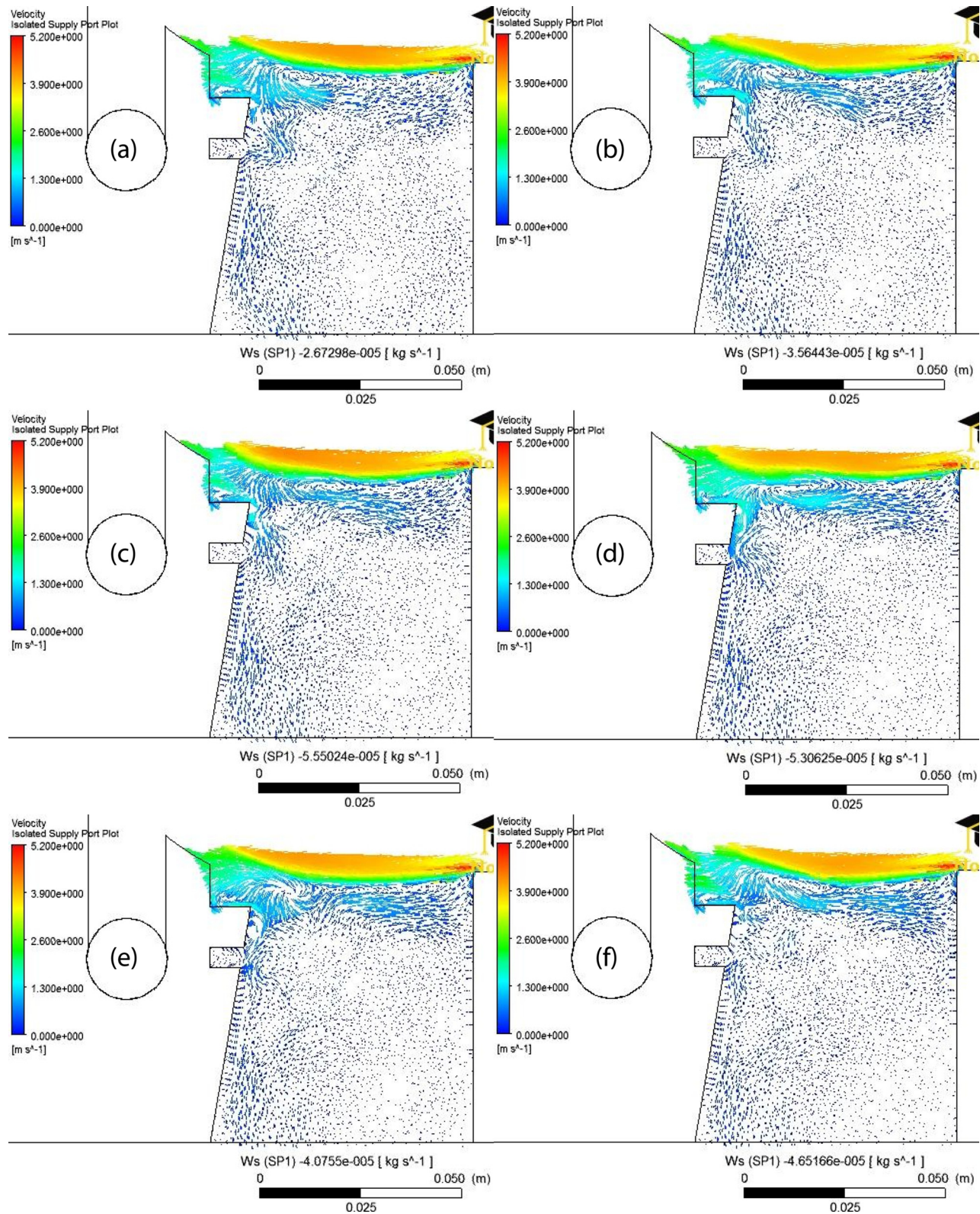
Fig. 8 Velocity vectors, geometry 2.2, SP1 ($P_c = -373$ Pa: z = -5mm): (a) 0.351 s; (b) 0.365 s; (c) 0.379 s; (d) 0.393 s; (e) 0.408 s; (f) 0.422 s

design. The device was similar to that used herein. In explaining the results of the visualization experiments Blanchard describes how, under pure control flow conditions, the fluid stream split at the top of the chamber with some of the flow being directed radially back through the supply port over the VXA's partition plate. With the net supply flow being negligible, an area of recirculation

within the supply port was observed. Blanchard then went on to explain how the same flow pattern was maintained as supply flow was increased, becoming gradually more unstable and oscillating between radial and reversed. Little importance was attributed to this flow formation by Blanchard, the focus of his investigation being the characterization of the VXA for ventilation control.
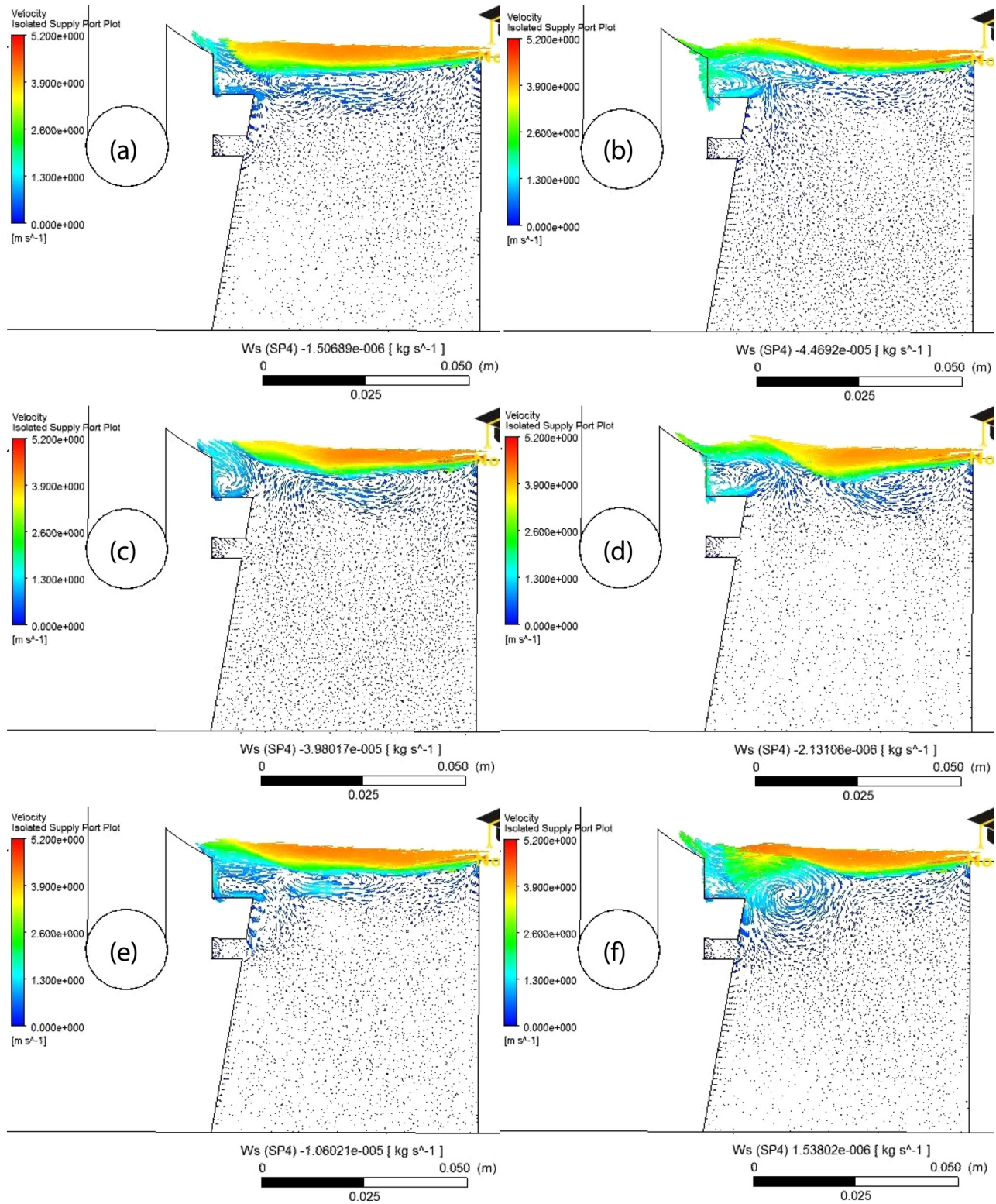
Fig. 9 Velocity vectors, geometry 2.2, SP4 ($P_c = -373$ Pa: z = −5mm): (a) 0.351 s; (b) 0.365 s; (c) 0.379 s; (d) 0.393 s; (e) 0.408 s; (f) 0.422 s

However, Blanchard's findings provide a clue as to the underlying cause of the VXA's poor performance.

3.3 Exit Port Perturbations. In order to visualize the fluid structures within the vortex chamber and exit port, a set of three-dimensional plots were created (Fig. 10) depicting reverse flow through the exit port outlet and based upon the q-criterion. Although they are essentially a qualitative representation, the plots clearly show a reverse flow area in the exit port and VXA throat, which changes with time. Each panel in Fig. 10 was created by specifying an iso-volume with reverse flow (i.e., a
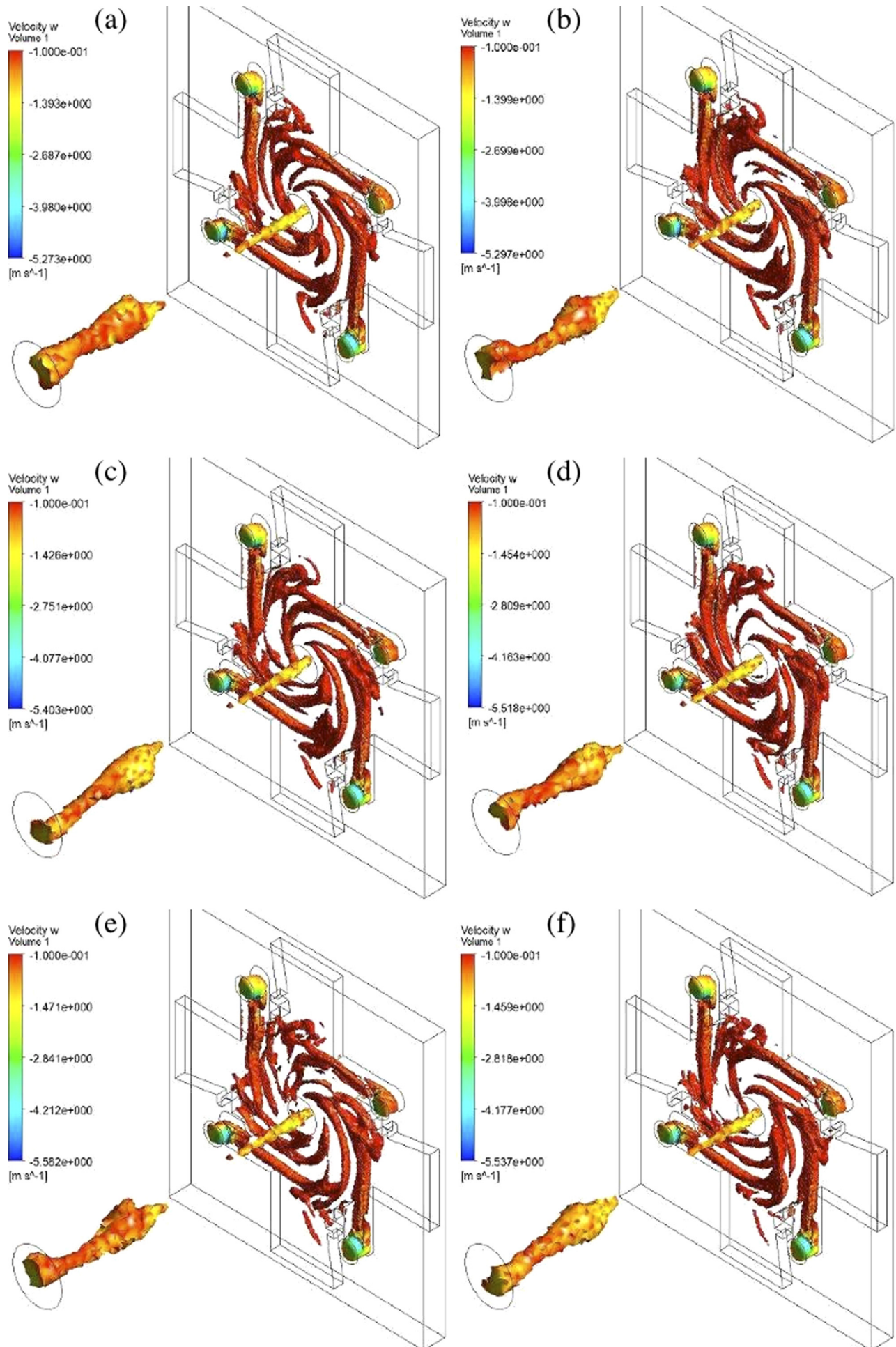
Fig. 10 Geometry 2.2, w and P vortex iso-volumes: (a) 0.350 s (b) 0.365 s (c) 0.379 s (d) 0.393 s (e) 0.408 s (f) 0.442 s

negative velocity component (w) in the z-axis). The external surface of the volume was then color-coded according to the value of w, by which means the changing structure of the reverse flow in the vortex core can be visualized.

The two distinct areas of reverse flow depicted in the isovolume, the exit port throat and the diverging section, suggest that close to the exit port throat the strength of the vortex centrifugal field generated is sufficient to reverse fluid flow in the core. As the vortex continues down the exit port, the tangential velocity reduces due to frictional losses. The reduction in velocity weakens the centrifugal field generated by the vortex; this causes the static pressure in the vortex core to rise, reducing and eventually preventing the formation of a reverse flow structure.

As the spinning flow moves down the exit port it enters the diverging section of the duct. The angle of the diverging section is severe, well in excess of the 7° recommended for VXA design. Static pressure recovery in this area is not instant; the still-spinning vortex flow expands into the larger extract duct causing the static pressure to fall once more. The reduced pressure field results in a larger area of reversed flow being generated. The gap between the two areas of reverse flow is where static pressure in the center of the vortex core increased due to tangential deceleration. There is no indication of reverse flow detachment from the rear wall of the VXA over the period simulated, this being one of the more significant causes of pressure and flow perturbations.

It is clear from Fig. 10 that flow through the exit port of the VXA under high swirl conditions is not axisymmetric. Although a full precessing vortex was not formed in these studies, there is clearly a time-dependent shift in the axis of the vortex toward the diverging section of the exit port duct. It is well known [11,19,20] that vortices can amplify small disturbances at their periphery (in this case, perturbations in the control or supply flow rates). It is possible that the small eddies shown in Figs. 6, 8, and 9 are coupling with the larger vortex in the chamber, creating the oscillations that are causing the shift in the axis of the vortex core (and ultimately in the variations of mass flow in the individual supply ports).

Similar studies were carried out on the alternative geometries 2.3, 3.2, and 3.3. All showed similar characteristics with respect to flow formation; however, none performed as well as geometry 2.2 with regard to prevention of back-flow.

4 Industrial Tests

The history of vortex amplifier assembly design for use on gloveboxes in the U.K. nuclear industry was given in Ref. [4]. The recent prototype tests demonstrating an improved performance as a result of reduced reverse flow are included therein. Two identical gloveboxes were used for prototype testing, each of which was manufactured from stainless steel with tempered glass sides front and back. The basic frame measured 1880 mm × 850 mm × 1100 mm with an internal volume of 1.703 m³ excluding gloves, the mini-VXA, and internal reinforcement. The VXA filter unit (including extract and control port filters) was mounted externally on the side of the glovebox and connected directly to the main extract header.

Prior to undertaking the investigation, oxygen sensors and the prototype VXA geometry were posted into each glovebox via the posting penetration or glove port. The prototype geometries were then mounted into the VXA sockets provided in each glovebox. Once installed, the glovebox was purged with nitrogen until both oxygen sensors read 0%. Once the glovebox was purged, the VXA was configured as it would be when operated under normal working conditions, i.e., a depression of 360 Pa in the glovebox.

During the tests the oxygen levels, supply flow rates, glovebox pressure, and VXA/extract filter pressure differentials were recorded every 5 min. Care was taken to ensure that flow rates and pressures remained constant throughout each test. The performance of each geometry was tested at two different nitrogen supply rates, i.e., 0.8 m³/h and 0.65 m³/h. In practice, nitrogen

flow rates in the region of 0.65 m³/h are used to achieve an oxygen concentration of 6% at the top of the glovebox.

The test results show that the new prototype VXA geometry 2.2 can reduce the back-flow of oxygen into the glovebox by up to 78% when compared to the current mini-VXA geometry (based upon a flow rate of 0.8 m³/h). At purge rates of 0.65 m³/h the prototype VXA geometries were found to be less effective, the rate of leakage from the units increasing by 16–20%. Despite the reduced performance, when tested under identical conditions leakage from the best of the prototype geometries is still 63% less than the current geometry used on site.

5 Conclusions

In this study the temporal effects of asymmetric flow in both the vortex core and supply ports have been simulated. Detection of these effects was unlikely in earlier VXA models. Unfortunately, the transient solution has not been run over a sufficiently extended time period and with enough time steps to capture a full period of asymmetric supply port flow structures. Nevertheless, the work supports Paper1 [2] by providing further qualitative evidence for asymmetry in the supply ports that may be associated with the precessing vortex. Moreover, although there is no field measurement with which to compare internal flow structures, the work further demonstrates the application of the computationally expensive BSL Reynolds stress model in a predictive mode when used to simulate flows in a complex three-dimensional geometry of narrow construction, with impinging control jets, a swirl chamber, and straight sharp-edged inlet ports,

Based upon the investigations described in this paper, the following conclusions can be made.

- When using the BSL Reynolds stress model with automatic wall treatment and restricted growth in boundary element thickness normal to the wall, evidence of asymmetric flows and a precessing vortex core has been captured in a VXA. Although internal swirling flow has been simulated in other engineering assemblies, this series of two papers is thought to be the first study to simulate flow with these asymmetric and cyclic effects in a vortex amplifier.
- When operated under high swirl conditions it is possible for aggregate supply flow through a radial VXA to be positive, whereas flow through individual radial supply ports is negative. The range of aggregate supply flow rates for the simulation was similar to that used in purged gloveboxes in the nuclear industry. From evidence herein, as well as in Paper1 [2], the authors believe this asymmetry is not solely due to vortex precession but results from a Coanda effect. The implication is that the BSL Reynolds stress model may have captured this Coanda effect.
- When operated close to its cut-off point, transient flow formations (recirculating eddies) in the VXA's radial supply ports can cause flow through the ports to reverse. The flow formations appear to be quasi-steady, having no definite frequency of repetition over the period simulated. This effect should be investigated with longer simulation times.
- A converging taper supply port geometry can be used to reduce the onset of supply port back-flow leakage from radial VXAs, the onset of bifurcated flow being delayed by the formation of small areas of recirculation at the top of the converging taper.
- VXA geometry 2.2 performed best in the parametric studies, the 10 mm × 10 mm section at the top of the taper generating strong recirculating eddies under high swirl conditions.
- Flow through the outlet and diffuser was also found to be nonaxisymmetric, with evidence for a precessing vortex core, which is related to the vortex in the VXA chamber, and hence to the back-flow asymmetry in the supply ports.
- Tests at the Nexia BTC facilities (now the National Nuclear Laboratory on the Sellafield site) show that the modified

geometry reduces the back-flow of oxygen into the glovebox by as much as 78% when compared to the devices currently in use. At purge rates of 0.65 m³/h leakage from the modified geometry was still 63% less than the control geometry when tested under identical conditions.

- Given the mechanisms responsible for supply port leakage, it is likely that other radial devices also exhibit similar supply flow characteristics when operated under high swirl conditions.

References

[1] Tippetts, J. R., 1984, "Finding the Operating Point of Eulerian Flow Machines," Int. J. Heat Fluid Flow, **5**(1), pp. 3–12.

[2] Parker, D., Birch, M. J., and Francis, J., 2011, "Computational Fluid Dynamic Studies of Vortex Amplifier Design for the Nuclear Industry—I. Steady-State Conditions," ASME J. Fluids Eng., **133**(4), 041103.

[3] Zhang, G., 2005, "Performance of Reduced-Scale Vortex Amplifiers Used to Control Glovebox Dust," Ph.D. Thesis, University of Central Lancashire, UK.

[4] Francis, J., Zhang, G., and Parker, D., 2012, "Vortex Amplifier Assemblies for Glovebox Applications Containing Radiological Hazard," Proc. Inst. Mech. Eng. E, J. Process Mech. Eng., **226**, p. 2.

[5] Schluter, J., Schonfeld, T., Poinsot, T., Krebs, W., and Hoffman, S., 2001, "Characteristics of Confined Swirl Flows Using Large Eddy Simulations," ASME Report No. 2001-GT-0060.

[6] Wegner, B., Maltsev, A., Schneider, C., Sadiki, A., Dreizler, A., and Janicka, J., 2004, "Assessment of Unsteady RANS in Predicting Swirl Flow Instabilities Based on LES Experiments," Int. J. Heat Fluid Flow, **5**, pp. 528–536.

[7] Turrell, M. D., Stopford, P. J., Syred, K., and Buchanan, E., 2004, "CFD Simulations of Flow Within and Downstream of High Swirl Lean Premixed Gas Turbine Combustors," *Proceedings of the ASME Turbo-Expo*, Vol. 1, pp. 31–38.

[8] Wang, J., Priestman, G. H., and Tippetts, J. R., 2006, "Modelling of Strongly Swirling Flows in a Complex Geometry Using Unstructured Meshes," Int. J. Numer. Methods Heat Fluid Flow, **18**(8), pp. 910–926.

[9] Woolhouse, R. J., Tippetts, J. R., and Beck, S. M. B, 2001, "A Comparison of the Experimental and Computational Modelling of the Fluidic Turn-up Amplifier at Full and Zero Swirl Conditions," Proc. Inst. Mech. Eng., **215**, pp. 142–152.

[10] Boucher, R. F., Boysan, F., and Haider, M. H. S., 1988, "Theoretical Computer Simulations of Swirling Flow in a Vortex Amplifier Chamber," Second International Symposium on Fluid-Control, Measurement, Mechanics and Flow Visualisation, pp. 370–374.

[11] MacGregor, S. A., Syred, N., and Markland, E., 1982, "Instabilities in Axial Vortex Amplifiers," Proceedings of the ASME Winter Meeting, 82-WA/DSC-7, pp. 1–4.

[12] Menter, F. R., 1992, "Improved Two-Equation k-ε Turbulence Model for Aerodynamic Flows," NASA Technical Memorandum No. TM-103975, Ames Research Center, Ames, IA.

[13] Menter, F. R., 1994, "Two-Equation Eddy Viscosity Turbulence Models for Engineering Applications," Am. Inst. Aeronaut. Astronaut. J., **32**, pp. 1598–1605.

[14] Wilcox, D. C., 1988, "Reassessment of the Scale-Determining Equation for Advanced Turbulence Models," Am. Inst. Aeronaut. Astronaut. J., **26**, pp. 1299–1310.

[15] Wilcox, D. C., 1994, "Simulating Transition of a Two-Equation Turbulence Model," Am. Inst. Aeronaut. Astronaut. J., **32**, pp. 247–255.

[16] Launder, B. E., and Spalding, D. B., 1974, "The Numerical Computation of Turbulent Flows," Comput. Methods Appl. Mech. Eng., **3**, pp. 269–289.

[17] Chow, S. K., 1968, "An Experimental Study on the Characteristics of Vortex Valves," Proceedings of the IFAV Fluidic Symposium, pp 1–11.

[18] Blanchard, A., 1982, "Some Characteristics of Fluidic Vortex Amplifiers in Ventilation Control," Design 82, Institute of Chemical Engineering, Symposium Series Vol. 76, pp. 210–219.

[19] Syred, N., 1969, "An Investigation of High Performance Vortex Valves and Amplifiers," Ph.D. Thesis, University of Sheffield, Sheffield, UK.

[20] Harvey, J. K., 1962, "Some Observations of Unsteady Flow Arising After Vortex Breakdown," J. Fluid Mech., **45**, pp. 82–84.